Chapter 2: Materials preparation

2.1 Materials selection

Two masterbatches were used in this study: Nanocor C30PE, purchased from Nanocor China, and Nanoblend 2101, from Polyone Corporation. They both consist of a polyethylene matrix (believed to be LLDPE) with a compatibilised MMT filler at a loading level of 38-42 %wt, although the similarity stops there. The organic modifier in the Nanocor product is octadecylammonium, whereas the Nanoblend 2101 is modified with dimethyl-di(hydrogenated tallow)-quaternary ammonium. These molecules are shown in Figure 2.1.

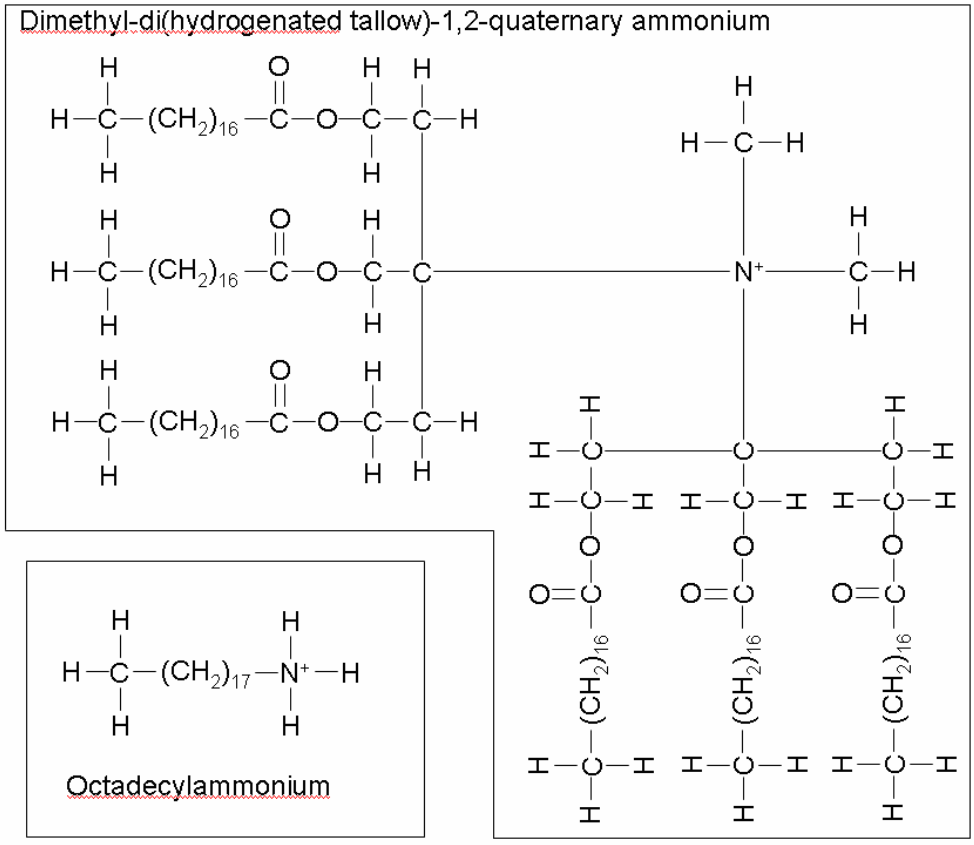

Figure 2.1: Chemical structure of the organomodifying surfactants used in Nanoblend 2101 (upper right) and Nanocor C30PE (lower left) masterbatches.

The inorganic clay: organic modifier ratio is 2:3 in the Nanoblend 2101, compared to between 3:7 and 35:65 in the Nanocor C30PE. The charge exchange capacities of the clays are also slightly different [2.1], and the relative contents of any heavy metal impurity ions were not known. Neither is it known to what degree the LLDPEs comprising the masterbatch matrices compare with each other in terms of either molecular architecture or maleic anhydride grafting level.* It is admitted that these uncertainties place limitations on the number of conclusions that can be drawn from this research; these are discussed in context in the subsequent chapters.

The LDPEs used were the low density LD100BW grade, purchased from Exxon Corp. and the high density Rigidex 160-25, supplied by British Petroleum. The blend compositions, prepared by single screw extrusion, are shown in Table 2.1

In addition to this, a reference blend was prepared with a deliberately poor level of dispersion. Nanocor I30P powder was used, which is the same organomodified MMT used in the C30PE masterbatch system. To prepare a solution blend, it is necessary to have both a solvent, in which the polymers will dissolve, and a non-solvent to precipitate-out the resulting blend. Provided they are miscible with each other, the solvent molecules will interact preferably with the non-solvent molecules, ejecting the polymer from solution. In this study, xylene was chosen as the solvent and methanol as the non-solvent.

100 ml of xylene was measured into a flask and heated on a stirrer mantle in a fume cabinet. 200 ml of xylene is able to dissolve a total of 2 g of polymer, which was weighed on a digital balance and added to the xylene along with a magnetic stirrer bar. Upon reaching boiling point (~140 ℃), the power to the mantle was reduced to keep the xylene boiling gently.

*Maleic anhydride imparts a polar nature to the polyethylene chains, increasing their compatibility with the MMT.

It took around 10 min for the polymer to dissolve completely, after which the solution was left to cool for 2 min before being added carefully to 100 ml of methanol. The resulting suspension was passed through filter paper and left overnight to dry. The filter paper was transferred to a vacuum oven at 40 ℃ for 48 h to remove the remaining solvent. It was necessary to clean the used flask by boiling a small amount of xylene in it.

Nomenclature	Number of parts by weight			
	LDPE	HDPE	Nanoblend 2101	Nanocor C30PE
NB0=NC0	90	10	0	0
NB5	90	10	5	0
NB10	90	10	10	0
NB20	90	10	20	0
NC5	90	10	0	5
NC10	90	10	0	10
NC20	90	10	0	20

Table 2.1: Extruded blend composition and nomenclature.

2.2 Extrusion

Extruders are used extensively in a wide range of industries from snack food to cable manufacture. Small-scale “microtruders,” however, are useful pieces equipment for the laboratory study of melt-compounding of polymers. A Randcastle RCP-0375 single-screw microtruder with a Recirculator^{TM} mixing section (see below) was used for this research. It is shown schematically in Figure 2.2. Pellets are fed into the hopper and are conveyed by the screw into the feed section. The machine relies on friction pumping, with the friction between the product and the barrel in the feed section being larger than the friction between the product and the screw. The pumping action of the feed section is therefore due to the pellets softening against the heated barrel wall.

In the compression section, the diameter of the screw root increases to accommodate the change in specific volume as the polymer melts. Screw designs can be tailored to specific polymers in light of this. For example, McCrum *et al.* [2.2] contrast a stepped screw, with a sharp transition in root diameter for nylon extrusion, with a more gradual PVC-optimised screw. As the thin film of molten material against the barrel wall thickens, it begins to flow downwards due to gravity. At the same time, the screw channel narrows, compressing the remaining solids against the screw wall. Viscous flow generates additional heat, accelerating the melting process. If the metering section provides sufficient back pressure, shear currents will begin to circulate, as shown in Figure 2.3(a). Alternatively, under starve-fed conditions, the situation shown in Figure 2.3(b) will develop and the extent of channel mixing will decrease. However, the residence time in the machine will increase which may be beneficial to mixing [2.3].

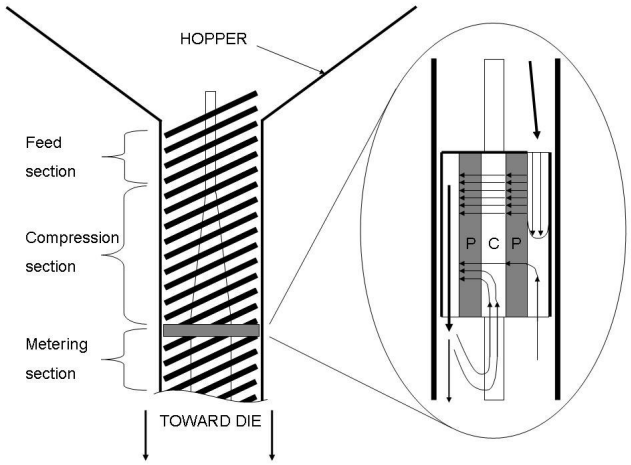

Figure 2.2: Schematic of a Randcastle single-screw extruder with Recirculator^{TM} mixing section.

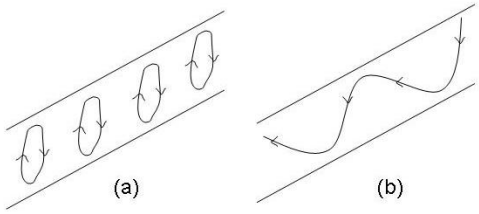

Figure 2.3: Dependence of circulating currents on back pressure. (a) Back pressure equal to pump pressure. (b) Zero back pressure. Adapted from McKelvey [2.3].

If the solids are not sufficiently compacted in the feed section, a melt film will not properly form in the compression section. The melting process will destabilise, resulting in temporary blockages and pressure surging further down in the metering section. The Randcastle RCP-0375 is fitted with a surge arrestor damper at the bottom of the metering section for this purpose.

Unlike twin-screw extruders, which employ mechanical rather than frictional pumping, single-screw machines are not capable of producing high levels of extensional flow. Dennis [2.4] discusses the fact that both shear and extensional flow are required for good nanocomposite dispersion. Extensional fields provide the forces necessary to break up the primary particles; the secondary particles are subjected to shear flow for subsequent redistribution. The Recirculator is therefore designed to supply the high extensional flow fields required for dispersive mixing in a single-screw context. As the polymer enters the Recirculator, it is subjected to a force along the axis of the Recirculator due to the low pressure encountered. This force is combined with a lateral force as the polymer is sucked by the first pumping island, into the second channel and immediately over into the third channel by the second pump, resulting in an extensional flow field. As the polymer leaves the Recirculator, some of it continues down into the metering section, but some of it is sucked back into channels 1 and 2 under low pressure.

It was necessary to wait for an hour for the extruder barrel to warm up. The set temperatures recommended in the manual were used: 177 ℃, 191 ℃, 204 ℃ and 204 ℃ for the feed, compression, metering and die sections respectively. The very top of the feed section was cooled to between 20 ℃ and 30 ℃ in order to prevent premature feedstock melting. It was found, however, that if the cooling temperature dropped below 15 ℃, condensation occurred which could be heard boiling deep inside the extruder. This could affect both the process stability and the clay chemistry, and so this situation had to be avoided. Upon reaching temperature, the screw was started and its speed slowly increased up to 50 rpm. Safety goggles and gloves were worn, and the drive motor ammeter was checked to make sure it did not rise above 2 A. The pressure in the compression section is not, according to the manual, permitted to exceed 4000 psi; in practice, pressures higher than 120 psi were never observed during the course of this research.

The pellets were too large for the extruder barrel. The solution employed by a previous researcher was to press a millimetre-thick sheet in a flat-plate press and cut it up into small pieces with a pair of scissors. Initially, this was thought too time-consuming. An alternative method was therefore tried in which the sheet was cut into 5 mm * 100 mm strips. The feed rate was poor, as this geometry proved unsuitable for friction pumping. Consequently, the extrudate was highly degraded. According to the manufacturer [2.5], there was a small chance that this colour could be explained by grease leaking from the pressure sensor, though optical microscopy demonstrated clearly that in our case the culprit was not grease but highly oxidised polymer. The output maintained a consistent grey colour even after several hundred grams of sheet were fed through the machine. The problem could only be solved by reverting to the original, laborious method of cutting millimetre cubes.

Since the clay in the masterbatch was already predispersed, it was not necessary to optimise the extruder operation for *ab initio* intercalation. Operating parameters were chosen for fastest throughput so as to minimise degradation: the maximum screw speed of 112 rpm, combined with flood feeding. The extruder was pre-flushed with 100 g of LDPE before processing 200 g of the above feedstocks in turn. (It was considered better to clean the machine by flushing with LDPE rather than stripping it down and cleaning it, since it was found that strip-downs still left oxidised fragments in the machine which would still require flushing on reassembly.)

Each blend composition emerged as a section of cylindrical extrudate approximately 2 m in length and 5 mm in diameter, which was subsequently sectioned at 10 equidistant points. In order to check for uniformity of composition, 5 mg of material was taken from each of these points and analysed by differential scanning calorimetry (DSC). This technique is described in detail in the next chapter. Melting endotherm analysis revealed that the high melting temperature peak area corresponding to the linear material reached its maximum within ~5 g of output material (which subsequently remained constant to within <10%), implying that the altering of blend compositions required the rejection of only small masses of material. Despite this, Luker [2.5] points out that a major scaling problem with laboratory-scale extruders is that inhomogeneities in feedstock compositions

arising from finite pellet sizes can pass straight through the machines to produce inhomogeneous product. Indeed, an initial trial extrusion of NC10 yielded subtle colour variations along the length of the extrudate in transmitted light. Although this could be explained by thickness variations, all extrudates were re-pressed, re-chopped and fed through the extruder a second time to achieve extrudates which were optically uniform.

200 μm thick samples were pressed from pieces of material sectioned at random points on the extrudates and analysed by optical microscopy. No evidence was found of non-uniform bulk dispersion. Comparison of material NB20 with the Nanoblend masterbatch did not yield any evidence of clay reagglomeration due to the extrusion process, although it was not possible to press samples directly from the Nanocor masterbatch due to its very high viscosity (see Chapter 5.)

Figure 2.4 shows a representative selection of extrudate samples produced during initial trials. Note the contrast between the dirty sample (strip feedstock) and the clean sample (cubic millimetre tablet feedstock.) The left hand sample illustrates the speed of transition from the LDPE flusher to material NC10. In order to be ultra-cautious with regard to the elimination of errors in blend composition, only the middle 50% of a 200 g sample was reclaimed for the second extrusion. A third pass was not deemed wise due to the risk of thermal degradation and loss of product.

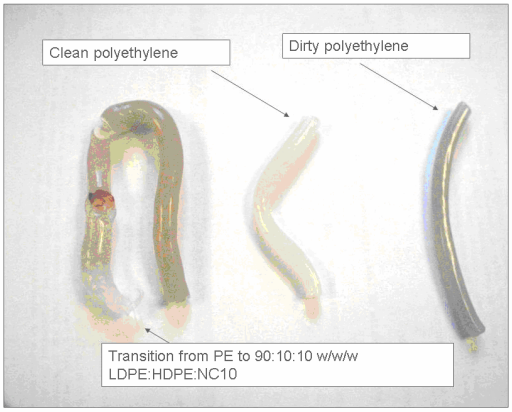

Figure 2.4: Photograph of extrudate samples from initial trials. The left hand sample demonstrates a quick transition from LDPE flusher to material NC10. A good sample contrasts with a highly degraded one due to poor friction pumping.

2.3 Wide angle X-Ray scattering (WAXS)

WAXS was used to gain confidence that the clay in the extrudates was sufficiently dispersed. This is a standard technique for the characterisation of MMT nanocomposites [2.6].

Hukins [2.7] has written a very readable introductory text on the subject. The key idea is that the spatial resolution that electromagnetic radiation can provide is limited by its wavelength. X-rays, having very small wavelength, are therefore able to interact on the molecular level with ordered structures to produce diffraction patterns. Whereas diffracted light can be focussed in an optical microscope to produce an image which is intelligible to the naked eye, the technology does not exist to refract X-rays in this way. The interpretation of X-ray diffraction patterns therefore requires great skill.

If we imagine two points sufficiently close together such that the incident X-rays can be considered as coherent, then we can define in Figure 2.5 an incident vector k_0, a scattered vector k and a scattering angle 2θ. It is then possible, with reference to the Ewald sphere, to represent the resultant beam as follows:

$$F(\overline{Q}) = \int_s \rho(\overline{r}) \exp(i\overline{r} \cdot \overline{Q}) \cdot d\overline{r} \qquad (2.1)$$

Where the integration is performed throughout the material and $\rho(\overline{r})$ is the electron density. The intensity of the beam is then the product of $F(\overline{Q})$ with its complex conjugate. As a result of this, a physical detector, whether a photographic plate or, nowadays, a phosphorescent target coupled to a CCD camera, cannot record phase information. This inherent loss of information, corresponding to the non-existence of a unique inverse of equation (2.1) is known as the "phase problem". Nonetheless, there has of late been some promising progress centred around the use of interfering reference beams to solve the phase problem [2.8],[2.9].

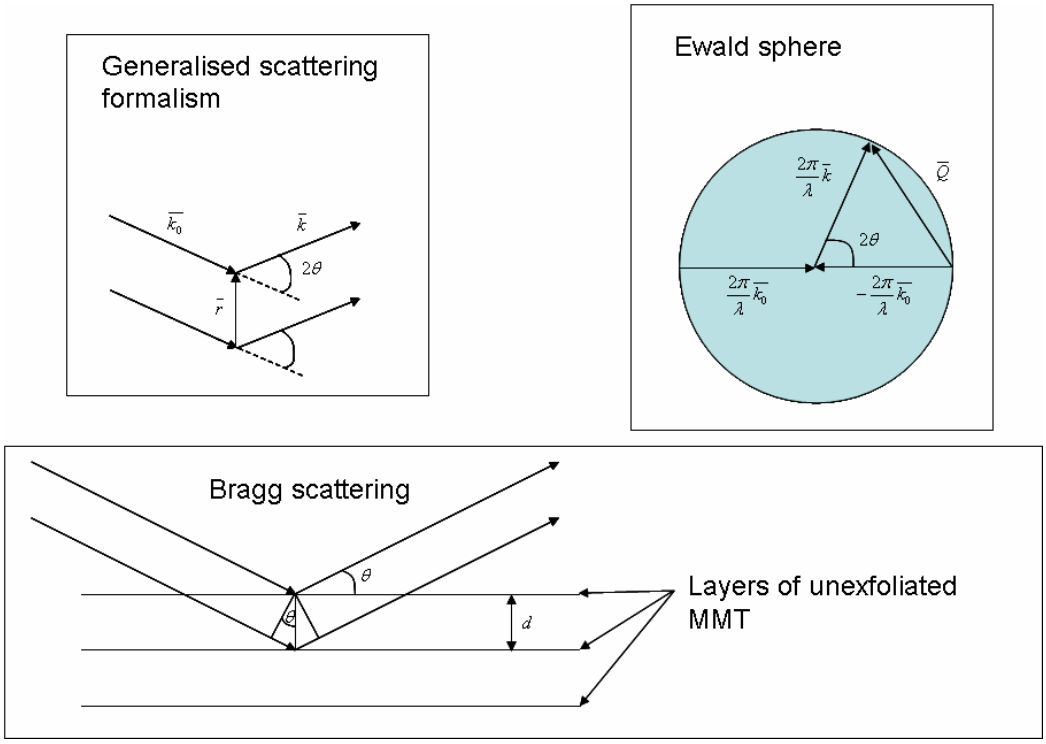

Figure 2.5: Schematic of WAXS optics. Top left: Generalised scattering from two points. Top right: Ewald Sphere. Bottom: Diffraction from Bragg planes.

Since, for this research, we are concerned only with studying the distance between parallel sheets, the Bragg equation is sufficient:

$$n\lambda = 2d\sin\vartheta \tag{2.2}$$

where λ is the wavelength of the radiation, d is the interplane distance and n is an integer. An X-ray tube was used at a potential of 30 kV and a current of 30 mA. Electrons which are thermionically emitted from a cathode are accelerated under vacuum towards a copper anode. There are 3 ways that the incident radiation can interact with the copper atom:

(i) through interaction with outer-shell electrons. This simply produces infra-red radiation and accounts for 99% of the energy of the system.

(ii) through interaction with atomic nuclei. This results in a broadband distribution of so-called Brehmstrahlung radiation and is useless to the crystallographer because it has no characteristic wavelength.

(iii) through interaction with inner-shell electrons. These give specific peaks – for copper, the K_α and K_β peaks. The K_α peak, corresponding to a wavelength of 0.154 nm was the one used for these experiments.

The data for this study were gathered using the equipment at the University of Reading. The radiation generated by the X-ray tube was filtered through a nickel filter and pyrolytic graphite monochromator to remove all non-K_α wavelengths. It was then passed through a 3-pinhole collimator to define a thin, parallel beam before passing through the sample. Initial experiments confirmed that 1 mm thick samples were perfectly satisfactory in terms of being sufficiently thin, so as not to absorb too much radiation, and sufficiently thick, so as to generate enough diffracted radiation to generate a diffractogram. An optimum thickness of 800 μm was found. A lead beam stop was placed on the detector side of the sample to prevent saturation of the charge coupled device (CCD) due to the undiffracted beam.

Since on a macroscopic scale, the samples could be considered as essentially random, their diffractograms were circularly symmetric. This meant that the signal obtained by taking a diametrical cross-section could be enhanced by integrating that cross-section through ±15°. Complete 360° integration was not possible as the centre point was difficult to locate precisely. This, together with spatial inhomogeneties in the CCD, would seriously affect the resolution of the cross-section. 255 CCD images were integrated to eliminate noise further. It was important to subtract the image obtained from sample-less chamber from the images due to the samples. This is because X-rays are scattered in air, and initial attempts at flooding the radiation path with helium were not successful.

Preliminary diffractograms, shown in Figure 2.6, were generated from NC10 and a poorly dispersed reference sample containing 15 %wt I30P. The latter material shows three main features. The two outermost rings correspond to the polyethylene <110> and <200> reflections [2.10]. These were used to calibrate the modulus of the scattering vector Q according to equation 2.3:

$$|Q| = \frac{2\pi}{d} \qquad (2.3)$$

Ring A indicates the spacing of the galleries in the clay. At this sample-detector distance, it is difficult to distinguish ring A from the unscattered beam leaking past the beamstop. Increasing the sample-detector distance revealed the gallery spacing to have a value of around 2.7 nm. Values for this parameter are reported to vary significantly within the range 1.2-3.7 nm, depending upon the functionalizing compound and its loading level [2.11-2.12]. Close examination of the image reveals a much fainter ring at ~1.5 nm which could be attributed to poorly functionalised clay. On the other hand, neither rings A nor D can be seen in the lower image, which is consistent with the hypothesis that the clay in these systems is well dispersed.

In order to minimise the chance of this being due to dilution effects, a poorly dispersed sample was prepared containing only 5 parts I30P. Intensity cross-sections were taken at 5 points, each separated by a beam width (1 mm). They are shown in Figure 2.7. Four of the traces are similar to each other and clearly distinguishable from the polyethylene reference trace. The fifth trace (unfilled circles) comprises a larger gallery peak intensity on top of a baseline which increases at low Q-values. It is possible that this corresponds to a higher local clay concentration superimposed on scattering at lower angles from attendant clustering interactions. If this is the case, the implication is that the other four traces correspond to a clay concentration even lower than 5 %wt, increasing the robustness of this method. Conversely, no confidence is lost if this effect is simply instrumental.

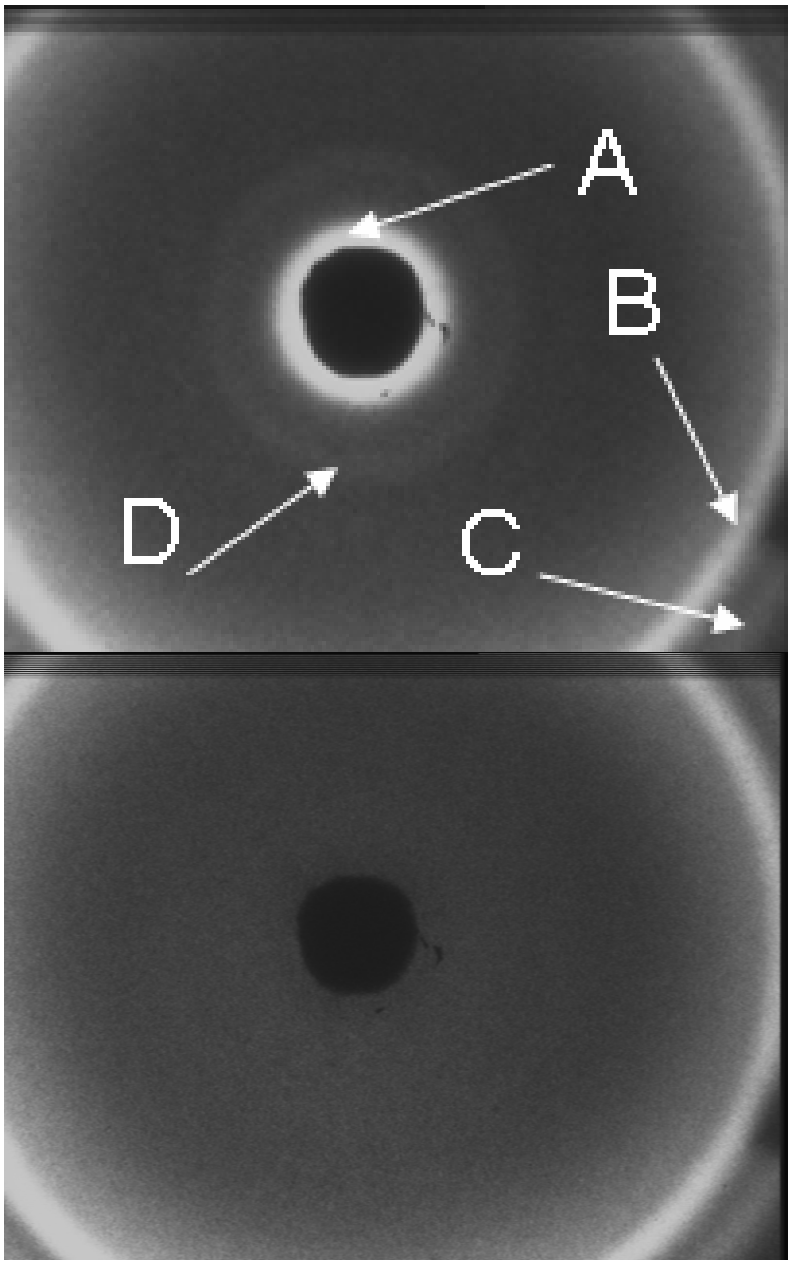

Figure 2.6: X-ray diffractograms of the poorly dispersed sample (upper) and NC10 (lower.) A corresponds to the o-MMT gallery spacing; B and C are the PE <110> and <200> reflections respectively. D may correspond to unmodified clay.

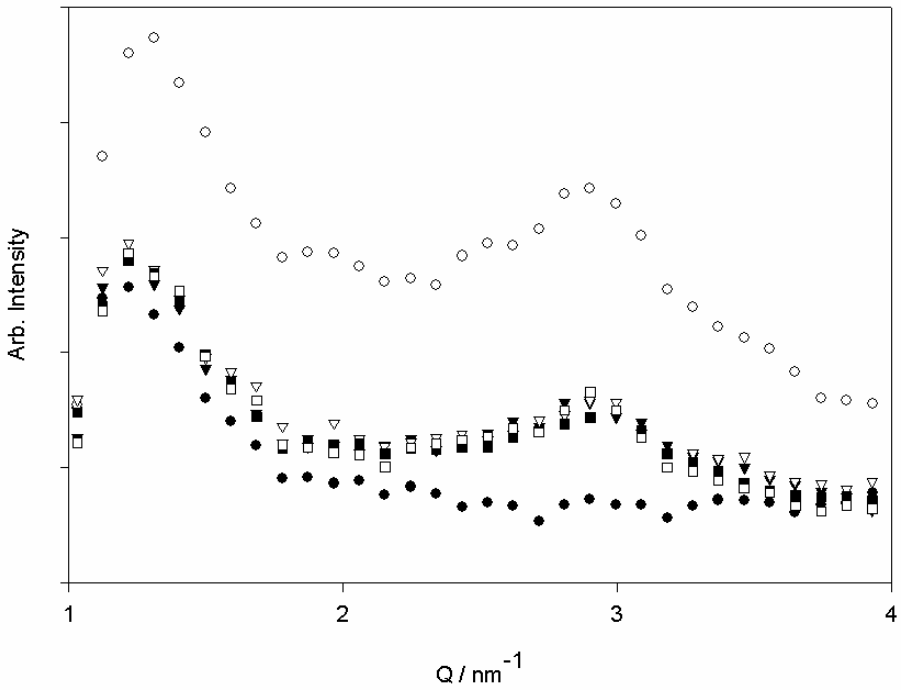

Figure 2.7: All symbols apart from black circles: four different intensity cross-sections for a xylene blended sample containing 90 : 10 : 5 w/w/w LDPE : HDPE : I30P powder. Black circles: unfilled reference. The intensity of the MMT basal spacing at Q = 2.9 nm^{-1} is seen to be spatially invariant.

The average of the four similar traces was used for comparison of the extrudates. These are shown in Figure 2.8, and likewise comprise several spatially-separated scans to minimise the risk of drawing illegitimate conclusions. From these data we arrive at the conclusion that there is no evidence that the clay is not exfoliated in the Nanoblend-based systems. However, there appears to be some positive evidence of intercalation in the Nanocor-based systems, arrowed in the figure. That this cannot be seen in NC5 may simply be a dilution effect. A minimum estimate for the characteristic length producing this feature is 3.5 nm^{-1}, or an increase of over 50% in the basal spacing.

It goes without saying that the disappearance of the original o-MMT peak does not necessarily imply exfoliation; it could equally indicate that the

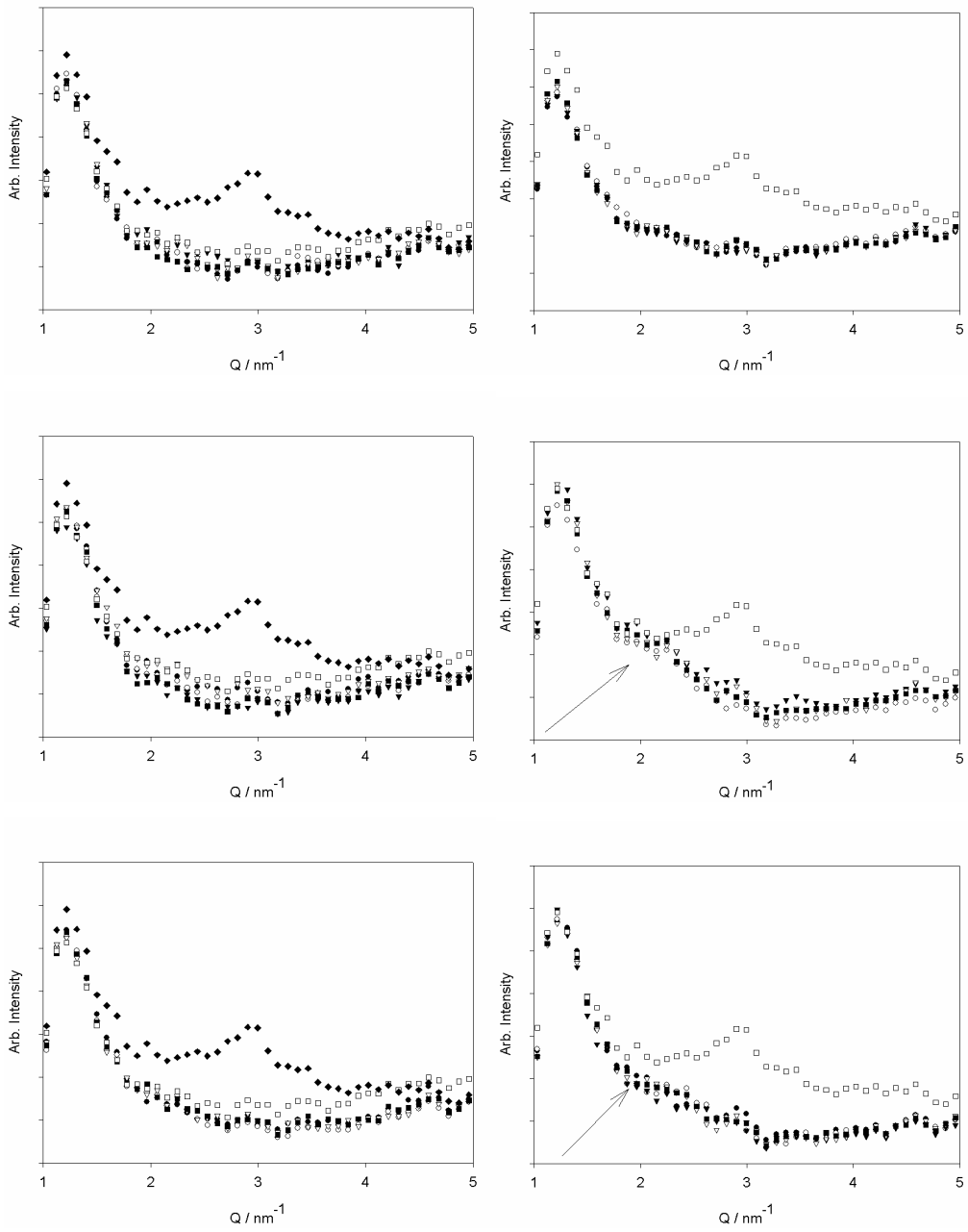

Figure 2.8: Intensity cross-sections for extrudates. Left-hand column: Nanoblend systems, Right-hand column: Nanocor systems. Loading level: 5 parts (upper), 10 parts (middle), 20 parts (bottom.) Poor dispersion reference signal from Fig. 2.6 included (upper traces.) Evidence of intercalation can be seen at low Q-values in both NC10 and NC20 (arrowed).

intercalated particles have become small enough to evade detection. There are a few examples in the literature of attempts to overcome this problem using small-angle scattering (SAXS,) but there are uncertainties associated with the modelling. Hernandez *et al.* [2.13] assume a simple distribution of tactoid sizes, with zero curvature and a uniform distribution in space. On the other hand, Causin *et al.* [2.14] do consider bending and Gaussian period distributions, but for infinite tactoids. Despite this, their extracted parameters do correlate very well with data obtained by transmission electron microscopy TEM.

Vonk [2.15] compared SAXS models for low crystallinity polymers. On the one hand, such models could consist of finite groups of perfect lamellae / amorphous sandwiches. For very low crystallinities, the inter-group electron densities could be considered as amorphous regions. Alternatively, in the space-filling limit, the external electron density would correspond to an infinite crystal. On the other hand, infinite sandwiches could be assumed under two types of distortion. A “distortion of the first type” corresponds to the case where the short-range order is smaller than the long-range order. This could be due to lamellar roughness. The second type corresponds to poorer long-range order due to curvature, such as is found in spherulites. Vonk concludes that in practice, both types of model are likely to fit the same data, with completely different conclusions. In the light of this, much caution needs to be exercised when attempting to model clay nanocomposites, where the kind of geometries encountered fall in between these idealistic cases.

2.4 Transmission electron microscopy (TEM)

TEM complements WAXS as a technique for characterisation of clay dispersions [2.16]. Electrons are preferable to light in terms of both their limiting resolution and the depth of field which they afford. These concepts are discussed in depth by Goodhew and Humphreys [2.17]. The diffraction limit of a wave is given by equation 4.1:

$$r = \frac{0.61\lambda}{\mu \sin\alpha} \qquad (2.4)$$

where *r* is the minimum distance at which two points can be distinguished, *λ* is the wavelength of the radiation, *μ* is the refractive index of the medium between the object and objective lens and *α* is the angle subtended by beam at the specimen. The depth of field, *h*, is then the range over which the sharpness of the image is not affected:

$$h = \frac{0.61\lambda}{\mu \sin\alpha \tan\alpha} \qquad (2.5)$$

Since the maximum wavelength of useful electrons is 0.01 nm and the minimum wavelength of visible light is 400 nm, the resolution of electron microscopes is much better. Electron microscopy also benefits from the large depths of field which result from having to keep *α* very small in order to minimise spherical aberrations in the lens system.

A glass knife was freshly prepared using an RMC glass knife maker. A cuboid of glass, 5 x 20 x 20 mm was clamped on its largest face in a purpose-built assembly. The glass was scored on the lower surface along 2/3 of a diagonal, and the mechanical pressure was slowly increased on this surface. A beam of light was shone through the glass, and pressure ceased to be increased when speckles of light became evident on the score line. After several seconds, such a speckle would develop into a crack which would progressively propagate through the sample, cleaving the block into two triangles. One of these triangles contained a fresh knife surface, on the edge containing the 1/3 of the diagonal which was not scored; the other contained an edge which was appropriate for initial microtoming but was not sharp enough for fine work.

Both blocks were mounted in a cryogenic assembly, together with the sample, connected to an RMC-7 microtome. LN_2 was pumped into the chamber and allowed to cool for 1 hr, ensuring that the knife and sample both reached -100 ℃. The sample was held by an arm which swept past the knife in a vertical arc. The arm was driven closer to the knife in 70 nm steps, removing material at 0.2 mm s^{-1} during each vertical sweep. In practice, not every cycle was successful in removing a slice of material, leading to slice thicknesses that are likely to have been between 100 and 300 nm. Only the

thinnest slices were suitable for TEM work due to high levels of electron absorption. A delicate balance was found in the number of cuts a fresh knife was capable of making. Any more than ~20 resulted in large sample thicknesses due to blunting. On the other hand, fewer cuts were not sufficient for obtaining thermal equilibrium between the knife holder and the sample. Sections were lifted from the knife surface using a 1 mm diameter thin copper loop on a wooden stick. The loop was immersed in water before being moved to the knife surface. Provided the water did not freeze, the sections were lifted off the knife by the water surface tension before being placed on a 400-mesh copper grid.

TEM images were obtained using a Jeol 3010 microscope at the University of Southampton and a Philips CM20 machine at the University of Reading. To minimise sample heating, the maximum acceleration voltage was used, which was 300 kV and 200 kV in the case of the Jeol and Philips machines respectively. In practice, only three samples each of NC20 and NB20 gave satisfactory images, the others being too thick. Nonetheless, the images were found to be consistent over each of these samples; any bias that exists in the samples is therefore due to selective factors in the microtomy process. For example, local clay concentration and orientation is likely to affect both the knife blunting process and the ability of the material to generate uniform, stress-free sections.

Unfortunately, it was not possible to obtain images at a magnification level commensurate with the WAXS data. In order to optimise the focus and stigmation, one must be able to discern a certain amount of structure. It is believed that the samples were too thick for a strong enough contrast mechanism to exist on the nanometer scale. Therefore, Figures 2.9 and 2.10, which show materials NC20 and NB20 respectively, are taken at an order of magnitude less magnification than initially desired. Even at this magnification, the samples are seen to be rather thick. It is tempting to attribute the holes (labelled A) in Figure 2.9 to large clay particles that have pulled out. However, these features may also arise from local stress concentrations. This hypothesis is supported by the blotchy nature of the background, and it is also consistent with data which will be discussed in chapter 5 to the effect that very high local stresses can be present in the highly filled Nanocor-based samples.

The feature labelled “A” in Figure 2.10 contains too much structure for a simple hole. Nonetheless, it indicates a highly localised low density region associated with stress concentrations and / or loss of clay. These features support the hypothesis that high levels of bias are indeed introduced into these sections by the microtomy process.

By combining the WAXS and TEM data, the following observations can be made:

● On the <10 nm scale, both the o-MMT in both the Nanocor and Nanoblend-based systems exists in an intercalated state. In NC20, the intergallery spacing may still be as low as 3.5 nm; it is higher in NB20.

● The intercalated clay is then associated in clusters at a range of hierarchical length scales. These range from stacks separated by 20-50 nm (features “B”) to clusters of stacks with characteristic sizes between 600 nm and 1 μm. As the images are 2-dimensional, it is not possible to discern to what extent the “B”-type features are truly independent objects or whether they are simply sections through “C”-type features. Nonetheless, the clay in NB20 is more localised in larger ~1 μm clusters, separated by distances of up to 1 μm, whereas clay in NC20 appears to be much more uniformly distributed.

● On the basis that the volumetric clay fraction in a 2D image will be roughly equal to the true 3D fraction raised to a power of 3/2, we can conclude that a large fraction of the clay is contained in these high-contrast clusters. Nonetheless, the blotchy composition of Figure 2.9 suggests that, at least in material NC20, this fraction is by no means 100 %.

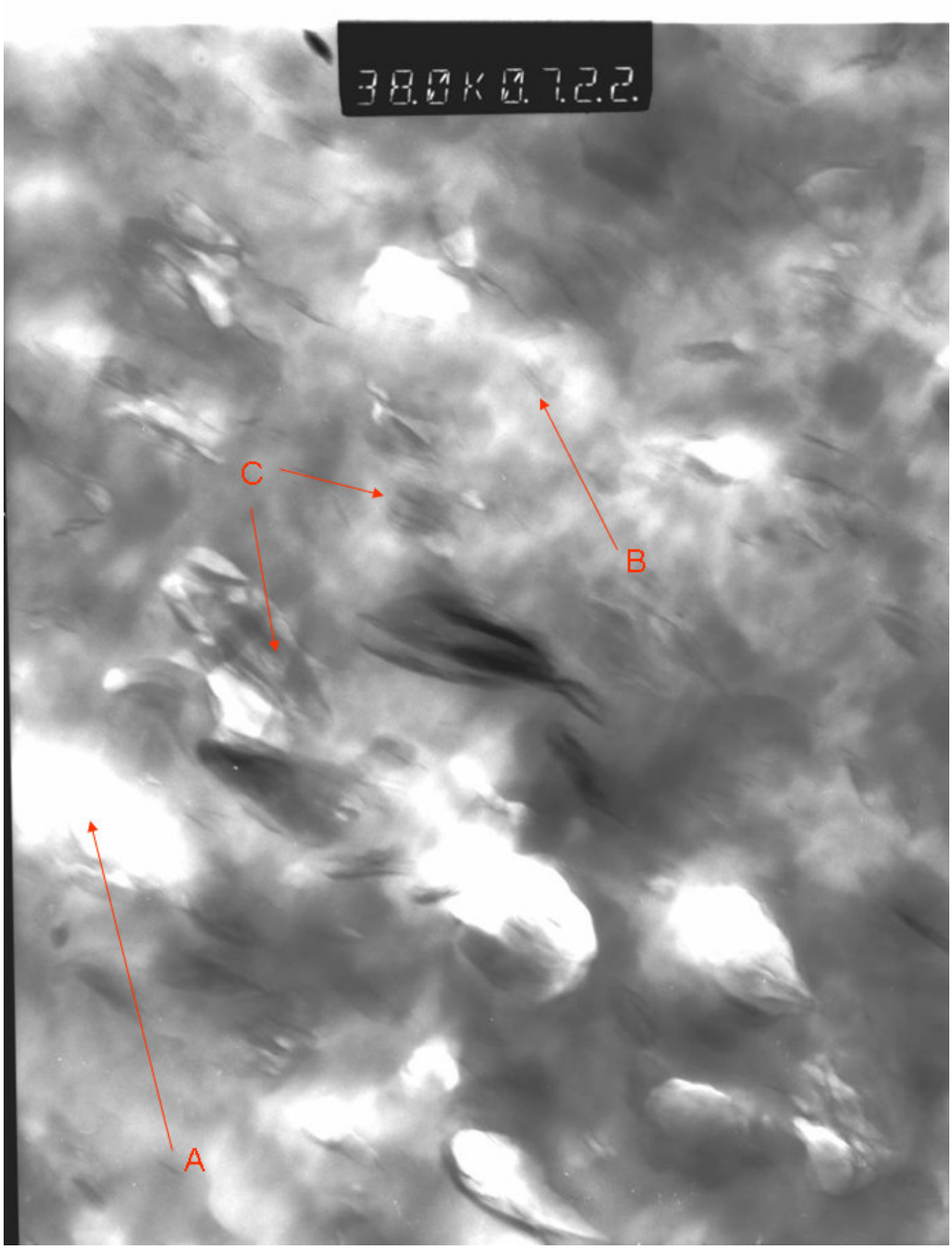

Figure 2.9: TEM micrograph of material NC20, using Philips CM20. A: Hole in sample. B: Single pair of intercalated stacks. C: Clusters of intercalated stacks. Width of information bar at top of image: 960 nm.

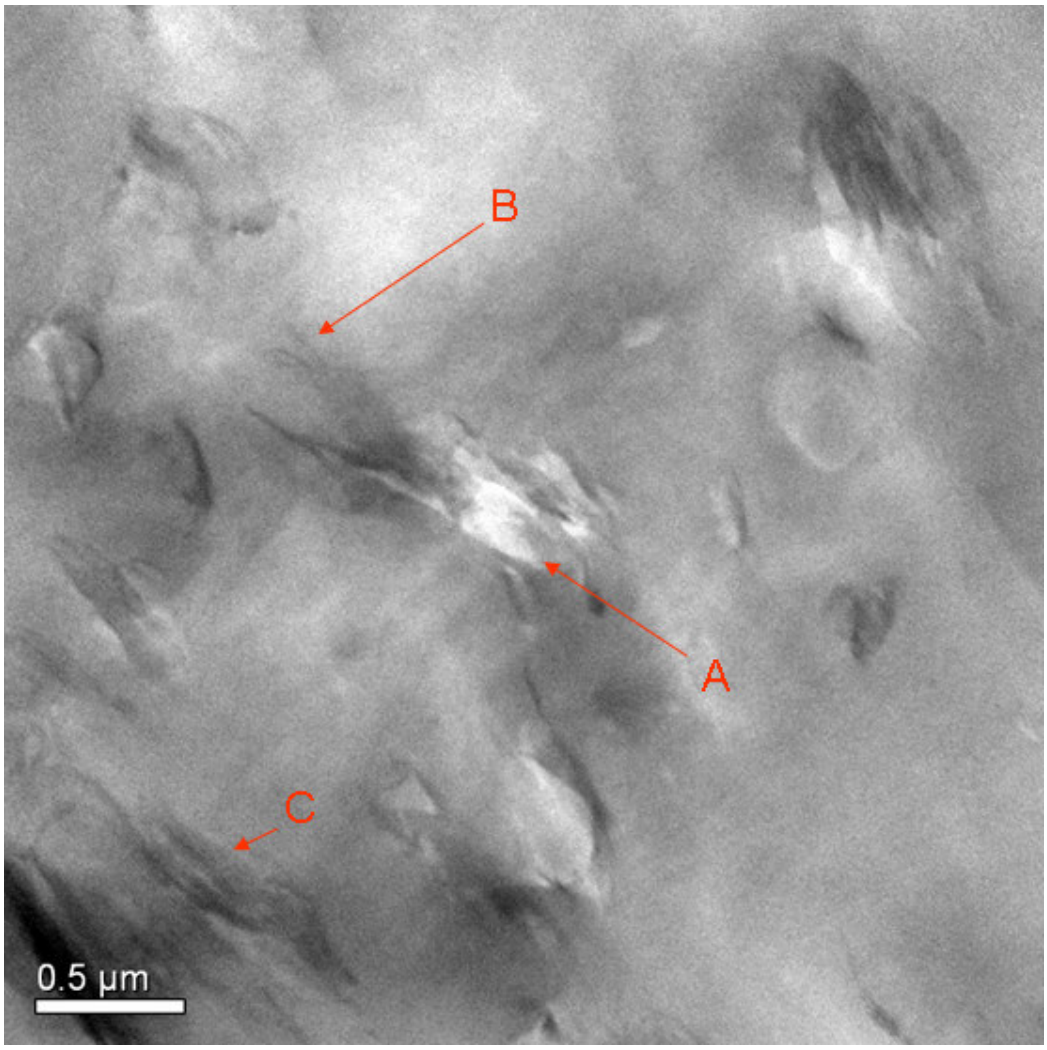

Figure 2.10: TEM micrograph of NB20, using Jeol 3010. A: Very thin region, possibly a hole. B: A pair of stacks. C: Large cluster of intercalated material.

2.5 Assessment of degradation

A first attempt at quantifying any thermal degradation during the extrusion process was made using Fourier transform infra-red microscopy (FTIR) [2.18]. When a beam of infra-red light is shone through a sample, the electric field vector couples with the valence bonds. The resonant frequencies of the bond vibrations then determine the characteristic wavelengths at which the electromagnetic radiation is absorbed. Broadband incident radiation is generated from a heated ceramic source, which then passes through the thin-

film sample to a half-silvered mirror. The beam is split into two orthogonal components which are subsequently reflected off a stationary and moveable mirror respectively. Upon recombining at the centre mirror, they interfere and travel to the detector. Translation of the moveable mirror generates an interference spectrum corresponding to the Fourier transform of the transmission spectrum. The absorption spectrum is then calculated by the software.

FTIR measurements were carried out using a Nicolet 710 spectrometer. The source was left to warm up for one hour at start up in order for the baseline to stabilise. A fresh baseline was collected after each sample, as it was known to drift. It was important not to breathe into the chamber when changing samples, as H_2O and CO_2 peaks would be introduced into the spectra. Each spectrum was normalised for residual baseline gradients and against the dominant polyethylene peak. A Graseby-Specac 25.011 hydraulic press with a thin-film die was used to make circular films ~70 μm thick and ~30 mm diameter.

Figure 2.8 shows the spectra obtained from the extrudates. Standard C-C and C-H peaks are seen in all of the traces. These are at 720-750 cm^{-1}, 1460-1490 cm^{-1} and 2850-2920 cm^{-1} respectively [2.19]. Standard Si-O-Si stretching behaviour associated with the clay is seen in the 1000 cm^{-1} region [2.20]. Other features seen only in the clay samples are seen around 500 cm^{-1} and 3800 cm^{-1} have been attributed to quarts impurities and “silicated skeleton” structures [2.20]. Furthermore, a peak is seen only for NC10 in the 3200 cm^{-1} region, which is possibly due to adsorbed water [2.21]. Dumais *et al.*[2.22] mapped the infra-red spectra of lightly aged polyethylenes. Carbonyl groups are located in the 1600-1800 cm^{-1} region, together with hydroxyl structures around 3400 cm^{-1} and (in the case of LDPE only) hydroperoxides at 3555 cm^{-1}. Background depressions due to C-O-C and C-OH groups are also expected to occur between 800 and 1300 cm^{-1}. The fact that none of these features can be seen in Figure 2.8 provides strong encouragement that the materials have not been significantly thermally aged by extrusion.

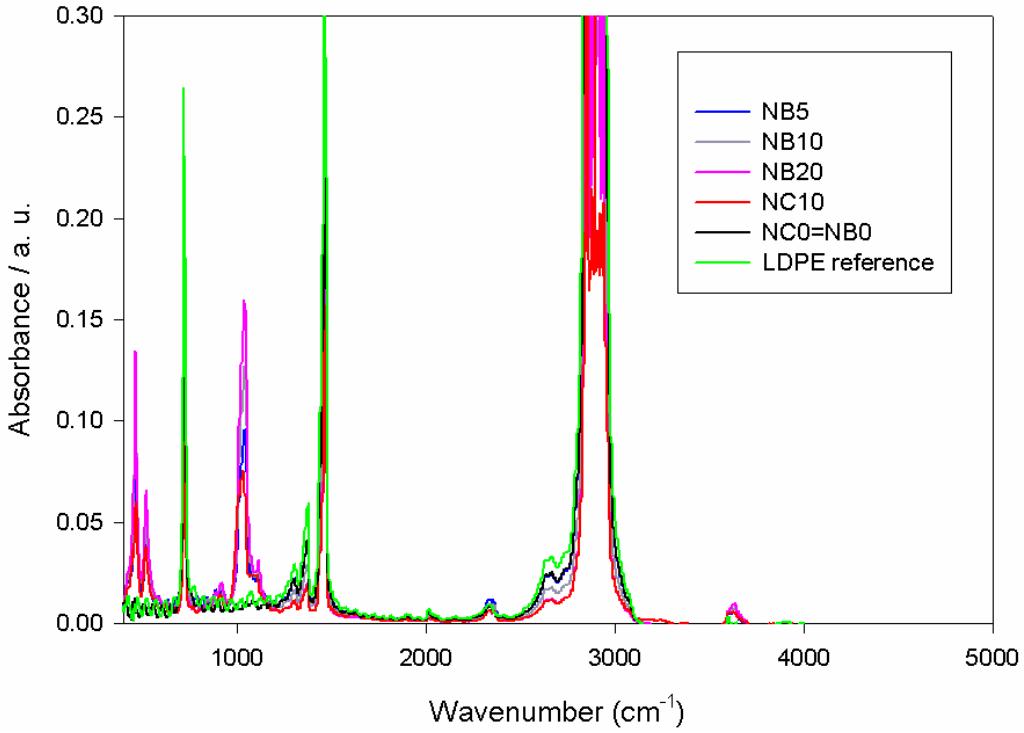

Figure 2.11: Comparison of Infra-red absorbance spectra from the extrudates. No evidence of thermal degradation can be seen.

Unfortunately, Figure 2.11 only permits us to conclude that the level of degraded moieties is < 1 % [2.23]. Raman spectroscopy, on the other hand, is much more sensitive to degradation. The Raman effect occurs when the polarisability of the bonding electrons is a function of position [2.24]. This gives rise to virtual states which facilitate the inelastic scattering of photons. The intensity of the scattered photons can be measured as a function of wavenumber shift, yielding information that complements FTIR. If there are fluorophores present in the material, fluorescence will occur. Usually, this is an inconvenience as the Raman-active signal is lost against a high-gradient background. For our purposes, however, the fluorescence trace serves as a useful indicator of degradation.

Non-confocal Raman spectra were obtained using a Renishaw Raman RM1000 system coupled to a Leica optical microscope. The spectrometer includes a Peltier-cooled CCD and a holographic notch filter to remove the

Rayleigh (elastically scattered) photons from the signal. A Renishaw 780TF NIR diode laser with a wavelength of 780 nm was used as the excitation radiation. This wavelength was calibrated using a silicon standard with a Raman peak at 520 cm^{-1}. The results were taken using an integration of two sweeps at a laser power of 10 mW. The data are shown in Figure 2.12, in which the characteristic polyethylene peaks are identified [2.25].

Although quantitative conclusions cannot be drawn from this technique, it does show that extrusion does introduce a small amount of degradation into the samples. Nonetheless, even the most degraded material, the "dirty polyethylene" of Figure 2.4, has a small fluorescence yield compared to the clay, suggesting that such optical probes might not be ideal for characterising this kind of degradation. UV-visible spectroscopy was also investigated as a technique, the results not shown here as they proved to be particularly insensitive to the level of degradation. Figure 2.13 is an optical micrograph of a 150 μm thin film pressed out of NB0=NC0. It shows that rather than being uniformly distributed throughout the sample, the degradation is present in clusters of up to 10 μm diameter. As the majority of the volume is undegraded, it is not surprising that the material is not amenable to characterisation by local optical probes. Quantitative degradation characterisation of these materials would therefore require knowledge of the degradation particle size distribution. This is beyond the scope of this work.

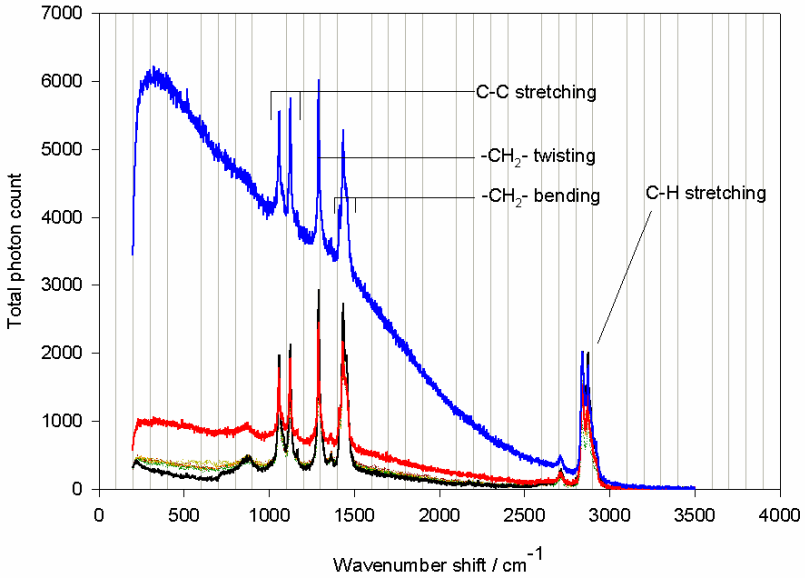

Figure 2.12: Nonconfocal Raman spectra for NB5 (blue plot), heavily degraded sample (red plot), unprocessed LDPE pellet (black plot) and 4 independent samples of NB0=NC0 (coloured dots). A significant level of fluorescence is seen in NB0=NC0 relative to an unextruded reference sample, implying a certain amount of degradation.

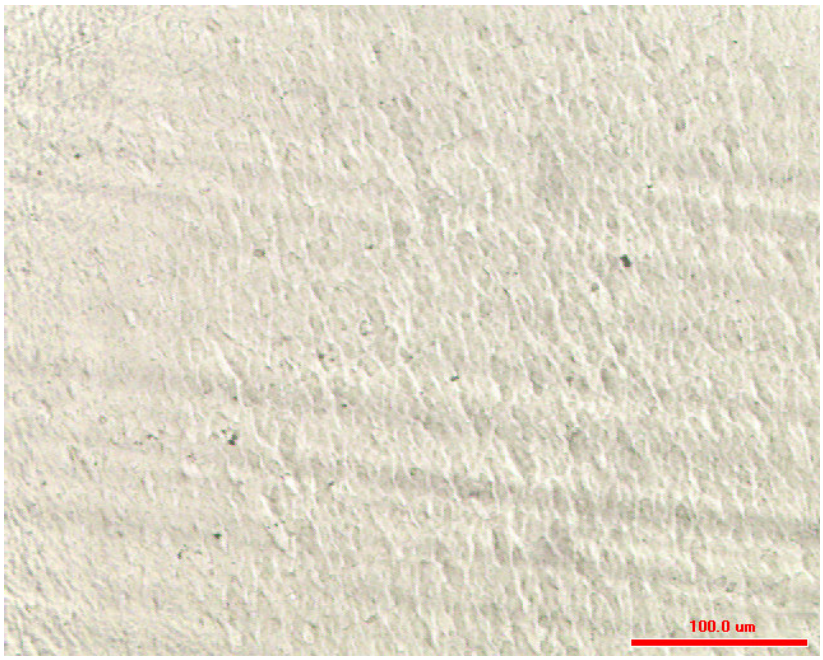

Figure 2.13: Optical micrograph of material NB0=NC0. Degradation is present in the form of sub – 10 μm inclusions.

2.6 Conclusion

A two-stage single-screw extrusion process has been successfully employed to produce blends of polyethylene together with various loading levels of o-MMT masterbatch. Fluorescence in the Raman spectra demonstrates that the extrudates are in fact lightly aged; if the fluorophores are associated with deep trapping, this is likely to have an effect on the high field behaviour of these materials. The HDPE: LDPE composition has been demonstrated to be invariant along the lengths of the extrudates. WAXS and TEM have been used to show that the clay in these materials exists in an intercalated state, although the apparent basal spacing in the Nanoblend-based materials is higher. The clay is mainly organised into alternating layers of polymer and clay stacks, with a periodicity of 20-100 nm. In NB20, these stacks are localised in ~1 μm clusters, whereas they are more uniformly dispersed in NC20. The clay distributions in the Nanocor-based materials are therefore very different to those in the Nanoblend-based materials. It is seen in Chapter 4 that differences in clay size distribution persist on scales commensurate with spherulite dimensions. The morphologies and engineering properties studied in subsequent chapters therefore compare the effects not only of clay chemistry and loading level, but also of particle size distribution on the macroscopic properties of these materials.